Research Square

Preprints are preliminary reports that have not undergone peer review.
They should not be considered conclusive, used to inform clinical practice,
or referenced by the media as validated information.

Can Hydroxyapatite Micro-Parts Be Mass-Produced by Vat Photopolymerization? Geometry Is Necessary, But Not Sufficient

Adel Badria

adel.badria@tuni.fi

Tampere university, Finland

Timo Laaksonen

University of Helsinki

Minna Kellömaki

Tampere university, Finland

Research Article

Keywords: ceramic vat photopolymerization, hydroxyapatite, micro-parts, debinding, co-sintering, process parameters

Posted Date: November 4th, 2026

DOI: https://doi.org/10.21203/rs.3.rs-11251196/v1

License: This work is licensed under a Creative Commons Attribution 4.0 International License.
Read Full License

Additional Declarations: No competing interests reported.

Can Hydroxyapatite Micro-Parts Be Mass-Produced by Vat Photopolymerization? Geometry Is Necessary, But Not Sufficient

Abstract

Mass production of discrete, sub-millimetre hydroxyapatite parts — called for as shape-engineered reinforcement in composites — is undocumented for ceramic vat photopolymerization, well established at centimetre scale. We report the fabrication and post-processing of hydroxyapatite cubes (1 mm design) and tetrapods (0.876 × 0.767 × 0.656 mm). Green parts released spontaneously from the build foil after 72 h at 40 °C, eliminating mechanical deplatforming with no measurable dimensional change. Co-sintering required no separation medium, with parts in mutual contact remaining free-flowing. Corner rounding of 23–34 % was already present in the green state, identifying it as a printing artefact rather than a sintering effect. Most consequentially, two batches from the same feedstock, furnace and thermal schedule reached 94.9 %TD (tetrapods) and 79.9 %TD (cubes); the tetrapod value sits within the supplier's own stated range for this material (94–97 %TD) while the cube value sits clearly below it. X-ray diffraction excluded phase composition as an explanation, confirming single-phase hydroxyapatite. The tetrapod encloses 77 times less material than the cube; since binder removal is diffusion-limited, the cube requires of order 35 times the debinding time. An independent, geometry-dependent exposure artefact reported here confirms that at sub-millimetre scale, process parameters are geometry-specific rather than size-specific, and that the ratio of enclosed volume to free surface — not nominal part dimension — is the governing quantity. Geometry-matched parameters are therefore necessary for mass production at this scale, but not sufficient alone: throughput economics and the absence of batch-level quality control remain separate barriers.

Keywords: ceramic vat photopolymerization; hydroxyapatite; micro-parts; debinding; co-sintering; process parameters

1. Introduction

Hydroxyapatite is the principal mineral constituent of bone, sustaining a long effort to shape it into synthetic bone substitutes [6]. Ceramic vat photopolymerization offers the greatest geometric freedom among printing routes, since each layer is defined optically [1], and commercial hydroxyapatite feedstocks are now available [2,3]. The process has been characterised in depth for this material class — cure depth and lateral overpolymerization set the achievable resolution [1], uncured-slurry removal has been examined for hydroxyapatite scaffolds [2], and sintering effects on densification and decomposition have been reported [3] — but this body of work shares an assumption: the object is a monolithic, centimetre-scale component printed singly, and the process questions follow from that premise.

A different requirement is emerging, in which the object is not one complex part but a large population of small ones: ceramic bodies below one millimetre, in quantities of thousands, with mechanical function encoded in their geometry, called for as shape-engineered reinforcement in architected composites [7] and as shape-specific functional particles [4]. Little of the established post-processing knowledge transfers, because the relevant quantities scale with part size — binder removal is diffusion-limited [8], the overpolymerized margin is fixed in absolute width

and so consumes a growing fraction of a shrinking feature [1], cleaning must remove slurry from between hundreds of closely spaced bodies [2], and whether discrete bodies bond during co-firing has no monolithic analogue [9]. These questions are not addressed in the literature for hydroxyapatite at sub-millimetre scale, and are not answerable from first principles, since the relevant limits are set by the interaction of a particular feedstock, machine and geometry.

This paper asks whether a ceramic vat photopolymerization system can meet this requirement, using two geometries — a solid cube and a thin-strutted tetrapod of comparable overall dimension — taken through cleaning, release, debinding and sintering. The comparison between them proves to be the most informative element of the work.

2. Materials and methods

2.1 Feedstock

LithaBone HA 480 M (Lithoz GmbH, Vienna, Austria), a hydroxyapatite slurry of solid loading 44.7 vol % (68.4 wt %) [12], theoretical density 3.156 g cm^{-3} (crystallographic value). The material batch corresponds to the currently qualified LithaBone HA 480 M grade, for which an expected relative density of 94–97 %TD at 1300 °C is specified [12]; full batch provenance in Supplementary S0.1.

2.2 Printer, geometries and nomenclature

Printing used a CeraFab 7500 (Lithoz GmbH). Two geometries were used: a cube (parent CAD edge 1.000 mm) and a four-armed tetrapod (parent CAD bounding box 0.876 × 0.767 × 0.656 mm, enclosed volume 0.0293 mm^3, struts far thinner than its overall dimension — a distinction central to §3.6). Parts were printed directly from the parent models with no additional scaling beyond standard shrinkage compensation (Table 1), confirmed by archived job files and by agreement between predicted and measured sintered dimensions (§3.2). The vat was heated to 40–50 °C against a specified 25 °C (Supplementary S0.2); the trade-off this entails is discussed in §3.7.

2.3 Process parameters

Table 1. Printing parameters, as used and as specified.

Parameter	HA 480 M specification [5]	This work	Note
Process temperature (°C)	25	40–50	§3.7
Layer thickness (µm)	25	25	—
Support structure thickness (µm)	300	300	—
Contour offset (µm)	0	0	—
Lateral (XY) shrinkage compensation	1.29	1.232	−4.5 %
Build direction (Z) compensation	1.33	1.259	−5.3 %
Dispensation correction (part / support)	1.2 / 1.3	1.500 / 2.000	—
Backlight exposure (s)	1.5	1.300	—
Settling time, start / general (s)	30 / 10	60 / 3	—
DLP energy, start (mJ cm^{-2})	180	100.032	deliberate, §3.4
DLP energy, general (mJ cm^{-2})	150	90.015	deliberate, §3.4
Number of starting layers	not specified	50	§3.4

The reduced exposure energy was adopted deliberately; reasoning and consequences are given in §3.4.

2.4 Build layout

Parts were nested on a build foil (LithaFoil; Lithoz GmbH), which increases adhesion of printed parts relative to a bare platform and is designated a primer in the supplier's documentation [5]; the mechanism is discussed in §3.4 (Supplementary S0.3 for full detail). Approximately 290 cubes were nested per build (Supplementary S1); part count was limited by the constraints in §3.8, not by platform area.

2.5 Cleaning and release

Parts were cleaned on the foil using a solvent-assisted air/LithaSol 80 protocol adapted for sub-millimetre parts, then the foil was released from the platform (full procedure in Supplementary S0.4).

2.6 Thermal release of green parts from the foil

The manufacturer specifies holding parts at 40–45 °C after cleaning [5]; foil removal before firing is mandatory, since the foil is not consumed and its presence causes cracking in larger parts [12]. Parts were held at 40 °C for 72 h, after which green parts released spontaneously with no mechanical handling. A candidate release mechanism, and its limitations, are discussed in Supplementary S0.5.

2.7 Debinding and sintering

A shortened thermal schedule was used (Table 2), omitting preconditioning and reducing dwell times, on guidance for parts of 200 µm [12]; the significance of this size mismatch is taken up in §3.6. Both batches reported here used this schedule, in the same furnace, in separate runs.

Table 2. Manufacturer standard and shortened thermal schedules.

Segment	HA 480 M standard [5]	This work
Preconditioning cycle	134 h (5.6 d), separate	omitted
25 → 430 °C (debinding)	82.7 h (dwells 5.8/10.5/7/7/7/6/6 h)	34.0 h (all dwells 1 h)
430 → 1300 °C	28.4 h (0.16 → 1.75 → 0.50 K min^{-1})	73.5 h (0.2 K min^{-1} throughout)
Dwell at 1300 °C	2 h	1 h
Cooling to 25 °C	11.0 h	24 h
Debind + sinter	122.05 h (5.1 d)	131.49 h (5.5 d)
Including preconditioning	256 h (10.7 d)	131.49 h (5.5 d)

2.8 Co-sintering arrangements

Three arrangements were compared using tetrapods: parts manually distanced with no separation medium (control), spread on a ZrO_2 powder bed, and fully embedded in ZrO_2 powder (grade BSZ3Y-W, Baikowski, nominal primary particle size 0.15 µm; full detail in Supplementary S0.6). Separately, a batch of approximately 1000 parts was co-sintered without separation medium.

2.9 Characterisation

Dimensions were obtained by digital caliper and rule-calibrated image analysis; automated segmentation was used only for scatter and counts, since it oversizes parts on over-exposed micrographs (Supplementary S0.7). Relative density was determined by micro-computed tomography (RX Solutions EasyTom S, isotropic voxel 13.222 µm) combined with mass on a four-figure balance, against 3.156 g cm^{-3}. Grey-value thresholds were set at the ISO50 value, the midpoint between material and air levels; full threshold-selection methodology, sample-holder exclusion, and uncertainty analysis are given in Supplementary S0.8 and S3.

2.10 X-ray diffraction

Phase composition was assessed by X-ray diffraction (Cu Kα) on sintered parts of both geometries, measured loose and unground; this affects peak intensity but not phase identification (Supplementary S0.9).

3. Results and discussion

3.1 Build occupancy

Approximately 290 cubes were nested per build (Supplementary S1), well below the platform's geometric capacity; the limiting constraints are discussed in §3.8.

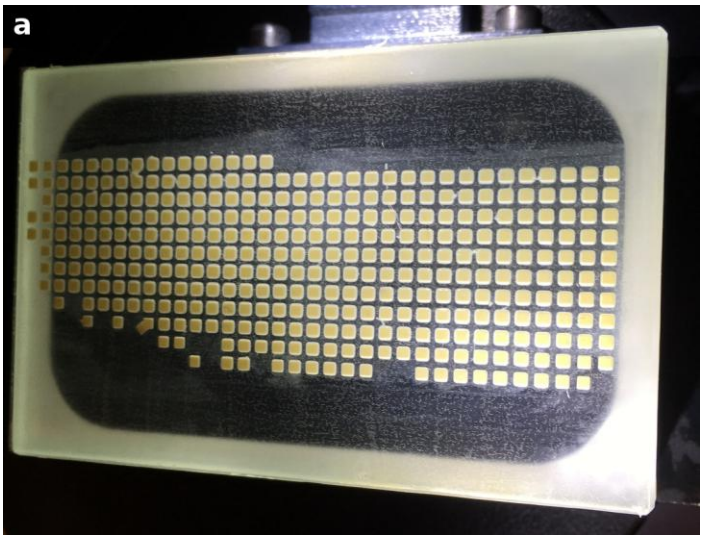


Figure 1. Populated build foil following a build of 1 mm cubes; approximately 290 parts nested in a regular array at ~2 mm pitch. The photograph carries no independent calibration reference; pitch is expressed relative to the measured green cube edge (Supplementary §S1).

3.2 Dimensional behaviour and measurement agreement

Sintered cube edge length was 1203–1206 μm by two independent methods — digital caliper and rule-calibrated imaging — agreeing to **0.2 %** (Supplementary S2.1). Green cubes measured 1310 μm against a compensated target of 1232 μm, a **6.3 % lateral oversize** consistent with lateral overpolymerization. Linear shrinkage was **8.3 %**.

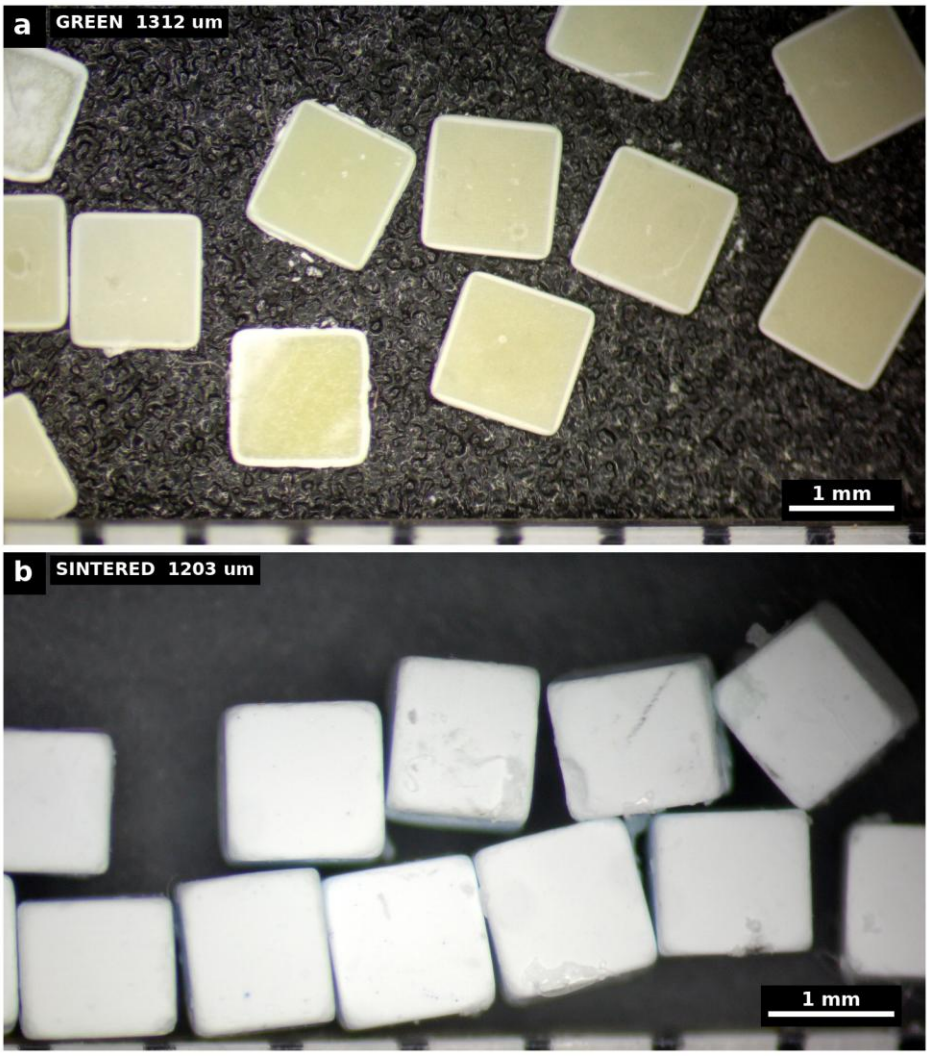


Figure 2. Cubes (a) in the green state and (b) after firing, each imaged with a millimetre rule in the field of view and cropped for presentation. Scale bars derived from the rule. Green 1312 µm, sintered 1203 µm — a linear shrinkage of 8.3 %.

3.3 Release from the build foil causes no measurable dimensional change

Green cubes measured on the platform before the 40 °C hold gave 1278 µm; after the hold and storage, 1310 µm — larger, not smaller, so any dimensional effect of release is bounded below approximately 2–3 % (Supplementary S2.3). This is the relevant result for a protocol being proposed for use: thermal release does not measurably alter part dimensions, though a small, unmeasurable contraction from interfacial debonding cannot be excluded.

3.4 A geometry-dependent exposure window

All tetrapod specimens showed base flattening; cubic specimens did not. The manufacturer's specified energy (180 mJ cm^{-2}) produced merged part feet and capillary-retained slurry at these feature sizes; exposure was reduced empirically to 100.032/90.015 mJ cm^{-2} (start/general), resolving the merging and consistent with independent guidance for parts this size [12] —

though the defects at the specified dose could also reflect capillary retention rather than lateral over-cure alone (concurrent chamber heating confounds attribution).

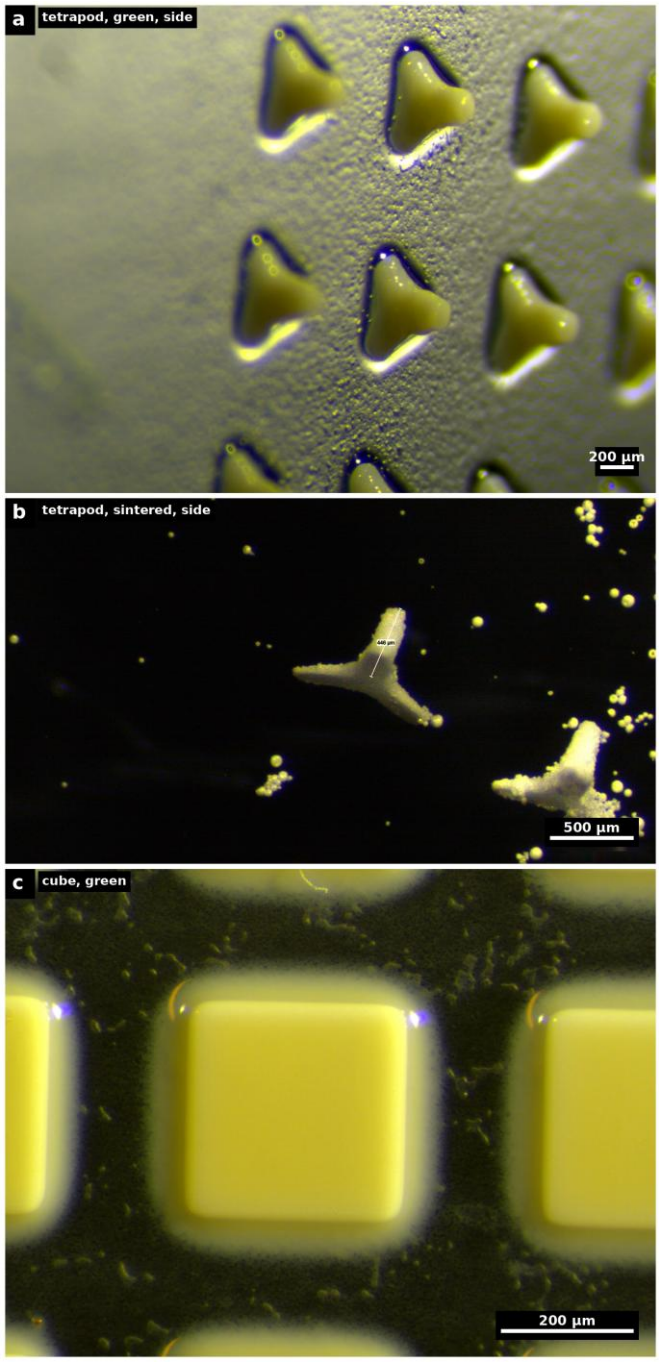


Figure 3. Base flattening in tetrapod geometries, present at both size scales: (a) green tetrapods, side view; (b) sintered tetrapods, side view. (c) A cube for comparison — the rigid flat base shows no equivalent deformation.

Reduced exposure produces correspondingly weaker green bodies; the tetrapod's three-arm base presents a small, mechanically weak contact area under the per-layer separation force,

whereas a cube's flat face is rigid. Exposure energy at this scale is thus bounded on both sides, and the viable window is geometry-dependent: the lower bound set by first-layer adhesion and green strength, the upper by loss of lateral definition; the window narrows as features shrink because the overcured margin is fixed in absolute width. The setting adopted here evidently lay within the window for cubes and below it for tetrapods, so a single exposure setting may not serve all geometries at a given size. Exposure was assessed at two dose levels only, so the window is bracketed rather than located.

3.5 Co-sintering requires no separation medium

Neither ZrO_2 arrangement — powder bed or embedded — conferred benefit over simple spatial separation, and both left adhered ZrO_2 particles on part surfaces; control parts were recovered clean, with no measurable distortion from the media (Supplementary S0.6). Adhesion occurs because, although the medium itself does not densify at 1300 °C, the hydroxyapatite surface is

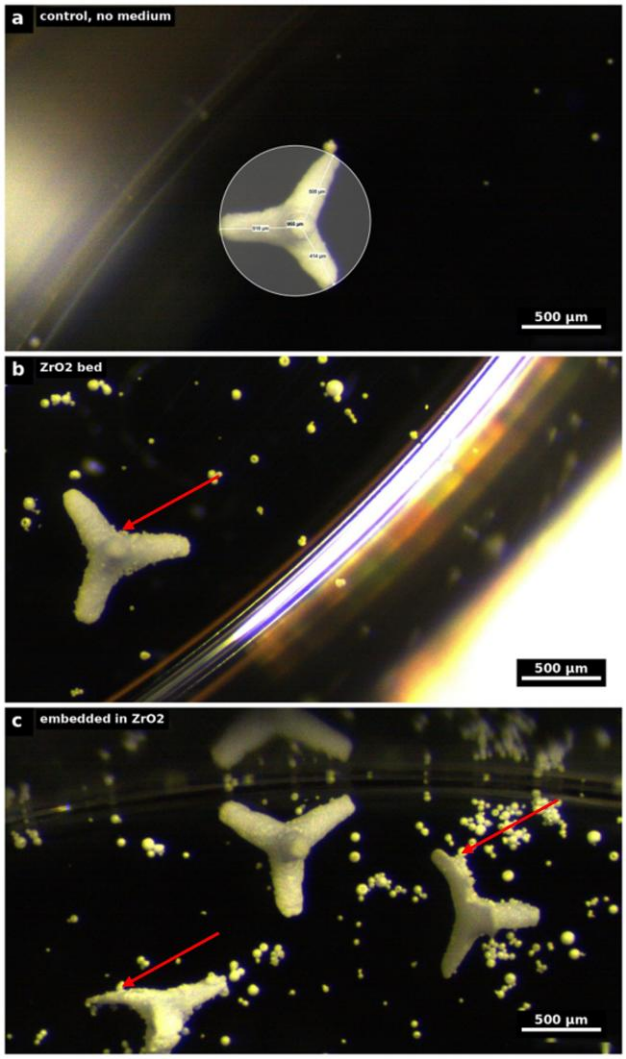


Figure 4. Co-sintering arrangements: (a) control, parts manually distanced with no separation medium; (b) parts spread on a ZrO_2 powder bed; (c) parts embedded beneath ZrO_2 powder. Arrows in (b) and (c) mark adhered ZrO_2 on part surfaces.

highly mobile at this temperature (≈0.84 of its melting point) and can flow around and key onto pressed particles; both candidate media also react chemically with hydroxyapatite, forming calcium zirconate or calcium aluminate respectively [10,11]. Alumina was not tested but is not predicted to be free of the problem on this reasoning; the appropriate choice at these part sizes is to use no separation medium at all. For a bioceramic intended for bone contact this is not cosmetic: 3Y-TZP is a non-resorbable phase that would alter the surface chemistry presented to cells and tissue.

Parts in mutual contact. A batch of approximately 1000 parts co-sintered without separation medium moved freely and individually on tilting the crucible after firing; the self-weight of a part this size would be supported comfortably by even a micrometre-scale sintered neck, so free motion indicates inter-part bonding did not occur. This is bounded by a ~3 µm optical resolution limit and by the shallow bed depth used (Supplementary S0.6); the batch depth at which the result holds is not established, and the geometry of this specific batch was not recorded, so it is most safely read as applying to the geometry and density regime it represents.

3.6 Densification differs substantially between geometries

This is the principal finding.

Both datasets were segmented by the same procedure: a threshold set at the ISO50 value determined from interior and exterior grey levels, with the sample holder excluded at the slice where the filled fraction of the vial cross-section reaches a plateau (§2.9).

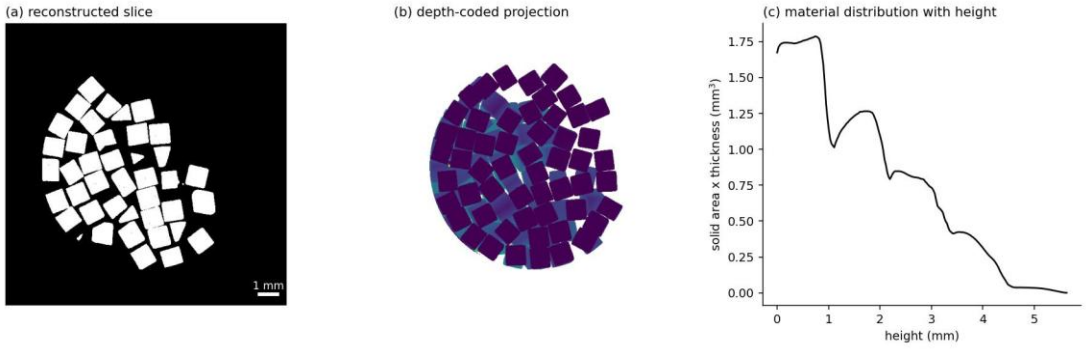


Figure 5. Micro-computed tomography of a sintered cube batch: (a) a reconstructed slice following exclusion of the sample holder; (b) depth-coded projection through the volume; (c) distribution of material with height. Isotropic voxel 13.222 µm; threshold at the ISO50 value (§2.9).

Table 4. Relative density by geometry, both determined by identical procedure.

	Ceramic level	Medium level	ISO50	Volume	Mass	Relative density
Tetrapods	22 267	19 049	20 658	13.351 mm^3	40.0 mg	94.9 %TD
Cubes	166.5	79.2	122.9	157.95 mm^3	398.2 mg	79.9 %TD

Corroboration and external benchmark. An independent segmentation of the tetrapod dataset agreed to **1.0 %** (95.9 %TD), and both values are stable against the processing decisions

available (Supplementary S3.3, S3.5). An expected relative density of 94–97 %TD at 1300 °C is specified for this material and applicable to this batch [12]; the tetrapod value sits inside this range, while the cube value sits clearly below it — a departure from what this specific feedstock is expected to achieve, not merely from an idealised standard. A weaker, independent check from first principles gives 96.0–98.9 %TD, consistent with the directly stated range (Supplementary S3.4).

The difference between the two geometries is therefore 15 percentage points (±3 and ±1 percentage points respectively; Supplementary S3.3, S3.5), measured by identical procedure on the same feedstock, furnace and thermal schedule.

The two geometries differ enormously in the quantity that governs binder removal: the amount of material each contains relative to its free surface.

Table 5. Geometric quantities governing binder removal.

	Tetrapod	Cube (green)	Ratio
Solid volume	0.029 mm^3	2.248 mm^3	77
Surface area	0.796 mm^2	10.297 mm^2	12.9
Envelope fill (solid / bounding box)	6.6 %	100 %	—
Surface-to-volume ratio	27.2 mm^{-1}	4.6 mm^{-1}	5.9
Mean distance to a free surface (V/S)	37 µm	218 µm	5.9

The tetrapod is predominantly empty space, enclosing 77 times less material than the cube; no point within it lies more than 37 µm from a surface, against 218 µm in the cube. Binder removal is diffusion-limited, so the requirement scales with the square of this escape path: the cube requires of order **35 times** the debinding time of the tetrapod. Expressed through the thickest section instead, the ratio is 5.6, a 32-fold difference — the two measures bracket the same conclusion. Incomplete binder removal leaves residual carbon that inhibits densification, and rapid gas evolution in an over-thick section generates internal microcracking; either produces a part that debinds sufficiently to appear intact but never densifies. A second, independent mechanism follows from the same geometry: a thin-sectioned body equilibrates with furnace temperature faster than a solid block, so under compressed dwells a solid cube may lag the programmed temperature while a tetrapod tracks it (not separately assessed). The shortened schedule was itself recommended for parts of 200 µm (§2.7); a 1.31 mm cube is 6.5 times thicker, a roughly 43-fold increase in debinding requirement, so the schedule was applied well outside the size range for which it was offered.

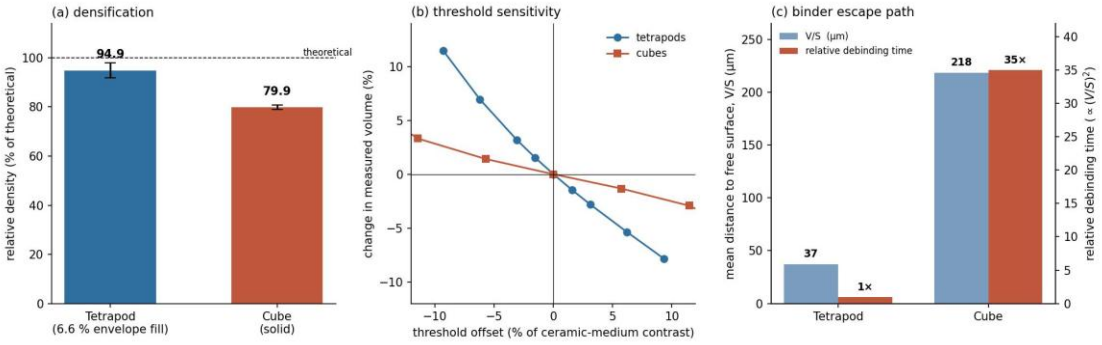


Figure 7. Densification by geometry. (a) Relative density determined from micro-computed tomography volume and mass; error bars are the threshold sensitivity given in §3.6. (b) Sensitivity of the measured volume to threshold offset, expressed as a percentage of the ceramic-to-medium contrast in each dataset; the tetrapods are the more sensitive, consistent with their higher surface-to-volume ratio. (c) Mean distance from an interior point to a free surface (V/S) for each geometry, and the resulting relative debinding requirement, which scales with its square.

The implication is the same as that of §3.4, arrived at independently and running in the opposite direction: one exposure setting was adequate for cubes and not tetrapods; one thermal schedule is adequate for tetrapods and not cubes. **Process parameters at this scale are geometry-specific: the governing quantity is section thickness, not nominal dimension.**

3.7 Elevated-temperature operation and its cost

Operating the vat above the specified 25 °C reduced slurry viscosity and improved fine-feature definition, but slurry underwent slow thermal polymerisation, progressively degrading a charge across successive builds; where material cost per build is already decoupled from product volume (§3.8), this compounds the economic penalty.

3.8 Practical limits on batch production

Batch size was limited by four factors unrelated to platform area: manual platform levelling (causing z-axis variation and part detachment), part detachment during dense packing (which scales adversely with part count), preprocessing software capacity, and absent integrated temperature control (Supplementary S0.10). A fifth, economic constraint dominates: a minimum slurry volume is required regardless of build size, so material cost per build is largely independent of part count — for a few hundred micro-parts of combined volume of order one cubic millimetre, essentially the whole cost of a vat charge is attributable to a negligible mass of product.

3.9 Cycle time

The shortened schedule is marginally longer than the manufacturer's for debinding and sintering alone (131.5 h against 122.1 h), but halves total processing time against the full specified route including preconditioning (10.7 days to 5.5 days). In light of §3.6, it should be regarded as validated only for thin-sectioned geometries.

3.10 Edge rounding originates in printing

Sintered cubes appear rounded rather than sharp-edged; two usual explanations — curvature-driven surface diffusion during firing, or optical blurring — do not apply, since substantial corner rounding (23–34 % of the edge, by two methods) is already present in the **green** state, before any thermal treatment. This is a printing feature: the ~40 µm projected DLP pixel corresponds to roughly seven pixels of lateral spread at this radius, consistent with scattering in a 44.7 vol % ceramic slurry extending the cured region beyond the projected boundary, and also accounts for the discrepancy between caliper and µCT volumes. Green faces additionally carry fine dark features (~7 % of projected area, ~2.9 µm median diameter) consistent with either hydroxyapatite agglomerates or entrapped air, optically indistinguishable and not resolved here.

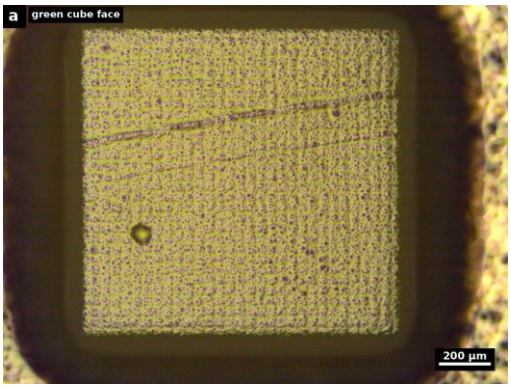


Figure 6. Reflected-light micrograph of a green cube face. Corner rounding is already present before any thermal treatment. The linear feature crossing the face is handling damage acquired during specimen preparation, not a processing defect.

3.11 Quality control and the limits of visual inspection

Defective and incompletely formed parts were present in every build (Figure 1); of one tetrapod batch, 381 of 392 identifiable fragments were intact tetrapods. No yield figure is reported: a slightly chipped arm cannot be reliably distinguished from an intact one by visual inspection at this size, and some breakage occurs only during post-processing handling, so process losses cannot be separated retrospectively from handling losses. Every handling step eliminated is therefore a yield step retained — a further argument for thermal release (§2.6) over mechanical deplatforming. More generally, no batch-level quality control exists for parts of this size: the density discrepancy of §3.6 was identified only retrospectively, by measurement rather than inspection.

3.12 Phase composition

Diffraction patterns from both geometries are consistent with single-phase hydroxyapatite. A uniform +0.24° 2θ offset between the two scans (Supplementary S4) was treated as an instrumental artefact — consistent with a sample-height difference between the loose, unmounted specimens — rather than a phase effect; after correction, every resolvable peak coincides. No feature is present at the CaO reference position (37.3° 2θ) in either pattern, excluding gross decomposition to free lime; a minor β-tricalcium phosphate contribution cannot be excluded due to peak overlap with hydroxyapatite. Phase composition is therefore excluded as

an explanation for the density difference of §3.6, consistent with the supplier's own unpublished observation that decomposition of this material is not significant at 1300 °C [12].

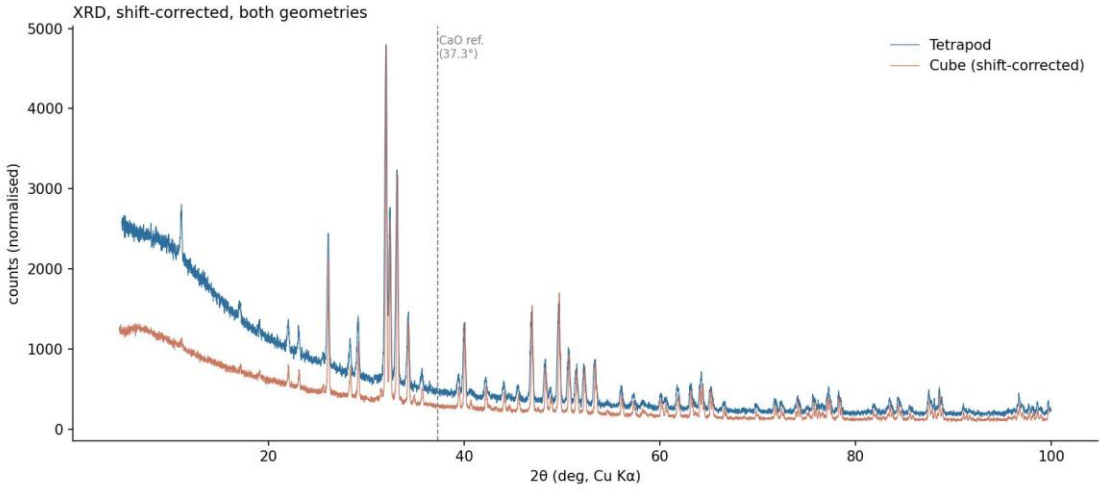


Figure 8. X-ray diffraction patterns for the tetrapod and cube batches, Cu Kα, after correction for the +0.238° 2θ offset between scans. Every resolvable peak coincides between the two geometries. The CaO reference position (37.3° 2θ) is marked; no feature is present above baseline in either pattern.

3.13 Implications

The correctable limitation is that exposure and thermal parameters here are geometry-specific; matching them to section thickness rather than nominal size would be expected to resolve both the base deformation of §3.4 and the densification deficit of §3.6. The structural limitations — manual levelling, absent temperature control, legacy software, and volume-independent material cost — mean throughput economics and the absence of batch quality control, not resolution, limit high-count production on this class of installation. This does not diminish the technique for rapid geometry screening at low part counts; for the transition to thousands of parts, current-generation systems or replication routes such as micromolding both warrant evaluation, each with its own constraints.

4. Conclusions

1. Green hydroxyapatite micro-parts release spontaneously from the build foil after 72 h at 40 °C — already specified for post-cleaning storage — eliminating mechanical deplatforming and its fracture risk, with no dimensional change detectable above ~2–3 %.
2. Co-sintering requires no separation medium: ZrO_2 powder adhered to part surfaces without benefit, and parts fired in mutual contact moved freely under gravity alone, bounded by shallow bed depth and a 3 µm optical resolution limit.

3. Corner rounding of 23–34 % of the edge length is present in the green state and is therefore a printing artefact, consistent with scattering-driven lateral spread of the cured region, not a sintering effect.
4. Two batches of the same feedstock, furnace and schedule reached **94.9 %TD** (tetrapods) and **79.9 %TD** (cubes), a 15-percentage-point difference (threshold sensitivities ±3 and ±1 pp). The tetrapod value is corroborated by an independent segmentation (1.0 % agreement) and by the supplier's stated range (94–97 %TD); the cube value sits clearly below it.
5. X-ray diffraction showed single-phase hydroxyapatite in both geometries with no evidence of CaO decomposition, excluding phase composition as an explanation for point 4; a minor β-tricalcium phosphate contribution cannot be excluded due to peak overlap.
6. Taken with the geometry-dependent exposure window of §3.4, process parameters at sub-millimetre scale are geometry-specific rather than size-specific; the governing quantity for thermal post-processing is the ratio of enclosed volume to free surface, not nominal part dimension.
7. Batch production was limited by manual platform levelling, part detachment, preprocessing software capacity and slurry economics — not by platform area.
8. **Limitations.** Single feedstock; the debinding hypothesis of §3.6 is inferred, not tested; the cube threshold sensitivity was determined from a re-exported greyscale volume in one of three cases, not the original; no yield figure could be established since intact and slightly damaged parts are not visually distinguishable at this size; inter-part bonding was assessed by free motion under gravity rather than electron microscopy, at shallow bed depth only; no mechanical or biological evaluation was performed; XRD phase identification is reported but quantification is not; the release mechanism and the foil's effect on adhesion were not independently confirmed; the upper bound of the exposure window was not diagnosed.

References

1. Zakeri S, Vippola M, Levänen E. A comprehensive review of the photopolymerization of ceramic resins used in stereolithography. *Addit Manuf* 2020;35:101177.
2. Ressler A, Zakeri S, Konnunaho P, Schwentenwein M, Levänen E, Frankberg EJ. Cleaning strategies for 3D-printed porous scaffolds used for bone regeneration fabricated via ceramic vat photopolymerization. *Ceram Int* 2024;50:53107-19.
3. Ressler A, Zakeri S, Dias J, Hannula M, Hyttinen J, Ivanković H, et al. Vat photopolymerization of biomimetic bone scaffolds based on Mg, Sr, Zn-substituted hydroxyapatite: Effect of sintering temperature. *Ceram Int* 2024;50:27403-15.
4. Kronenfeld JM, Rother L, Saccone MA, Dulay MT, DeSimone JM. Roll-to-roll, high-resolution 3D printing of shape-specific particles. *Nature* 2024;627:361-8.
5. Lithoz GmbH. Material Process Parameters: LithaBone HA 480 M. FORM 201.90, Process Parameter Sheet V 20.
6. Dorozhkin SV. Bioceramics of calcium orthophosphates. *Biomaterials* 2010;31:1465-85.

7. Singh A, Karathanasopoulos N. Mechanics of ceramic-epoxy interpenetrating phase composites engineered with TPMS and spinodal topologies. *Compos Sci Technol* 2024;253:110632.
8. Trunec M, Cihlář J. Thermal removal of multicomponent binder from ceramic injection mouldings. *J Eur Ceram Soc* 2002;22:2231-41.
9. German RM. Sintering Theory and Practice. New York: Wiley-Interscience, 1996.
10. Castkova K, Hadraba H, Matousek A, Roupcova P, Chlup Z, Novotna L, et al. Synthesis of Ca,Y-zirconia/hydroxyapatite nanoparticles and composites. *J Eur Ceram Soc* 2016;36:2903-12.
11. Akmal M, ul Hassan M, Afzal M, Ryu HJ. Novel approach to sintering hydroxyapatite-alumina nanocomposites at 300 °C. *Mater Chem Phys* 2021;260:124187.
12. Lithoz GmbH, personal communication

Supplementary Files

This is a list of supplementary files associated with this preprint. Click to download.

- HAmicropartsPIAMSupplementaryv2.docx